Available online at www.sciencedirect.com
ScienceDirect
Journal of Sound and Vibration 323 (2009) 626–644
JOURNAL OF SOUND AND VIBRATION
www.elsevier.com/locate/jsvi

Reconstruction of distributed dynamic loads on a thin plate via mode-selection and consistent spatial expression

X.Q. Jiang, H.Y. Hu*

MOE Key Lab of Structure Mechanics and Control for Aircraft, Nanjing University of Aeronautics and Astronautics, 210016 Nanjing, China

Received 6 July 2008; received in revised form 5 January 2009; accepted 6 January 2009
Handling Editor: J. Lam
Available online 13 February 2009

Abstract

This paper presents a convenient and efficient approach to reconstruct two-dimensional distributed dynamic loads on a damped thin elastic plate from its steady-state dynamic response. The approach is based on a mode-selection method which comes from an idea that an optimal range of frequency and mode exists for dynamic load reconstruction, as well as on the consistent spatial expression of the distributed dynamic loads. The criterion for mode selection is derived theoretically. A comparison between the method of truncated singular value decomposition (TSVD) and the method of mode selection demonstrates that the former is unstable while the latter is not only stable, but robust. With the proposed criterion, the method of mode selection enables one to find an optimal range for load reconstruction provided that the error bounds of both parameters and objective are given or estimated, and hence to make a balance between the reconstruction range and the error control.

1. Introduction

To reconstruct dynamic loads from response on a structure is of great practical interest in aerospace engineering, mechanical engineering and civil engineering, because a prior estimation of the dynamic loads will make the design, analysis and evaluation of the structure more efficient and less costly, while direct measurements of the dynamic loads are not feasible in many practical cases. The past decade has witnessed numerous studies of identifying the dynamic loads on a system of multiple dof [1–4], the moving loads on a bridge [5,6], and impulsive load or multi-point load on a continuum [7–9]. Nevertheless, the reconstruction of spatially distributed dynamic loads on a continuum is relatively new and few [10–15]. For instance, Liu and Shepard [11] studied the reconstruction of harmonic forces applied on a beam, while Granger and Perotin [14] investigated the identification of the random excitations on a beam. In those two studies, they introduced and applied similar but different modified modal expressions for beam dynamics. Pezerat and Guyader [13] studied the reconstruction of harmonic excitations acting on a rectangular plate, and Djamaa et al. [10] studied the loads on a thin cylindrical shell. In both studies, they employed the mode superposition method and finite

*Corresponding author. Tel.: +86 25 8489 1672; fax: +86 25 8489 1512.
E-mail address: hyhu@nuaa.edu.cn (H.Y. Hu).

0022-460X/$ - see front matter © 2009 Elsevier Ltd. All rights reserved.
doi:10.1016/j.jsv.2009.01.008

difference scheme for derivative calculation to describe the plate or the shell. Sehlstedt [12] investigated a seemingly different problem of reconstructing the boundary traction on a constrained structure. Furthermore, Jiang and Hu [15] proposed an approach to reconstruct the distributed dynamic loads on an Euler beam from its steady-state response.

When the model of multiple dof and the multi-point excitation model fail to work and meanwhile direct measurement for distributed dynamic loads is not available, it is especially valuable to reconstruct the distributed dynamic loads on a continuum. However, this is a complex inverse problem with inherent ill-posedness. In some studies mentioned above, much attention was paid to the complicated technical problems in mathematics, especially in the ill-posedness and regularization methods [16–23], whereas discussions on the physical nature of the problem are not enough.

In this paper, it is proposed and demonstrated that this ill-posedness basically comes from physics, instead of mathematics. From a viewpoint of the forward problem from dynamic load to dynamic response, the continuum acts as a transducer with inherent smoothness physically. Consequently, in the load reconstruction problem the continuum behaves like an inverse transducer that enlarges the unevenness in response information. This fact apparently suggests that the reconstruction of distributed dynamic loads on a continuum based on the mode superposition can be solved only in a finite domain of modes and frequencies. This idea consequently leads to the proposition of a method of mode selection, which was first demonstrated in the authors' previous work [15].

Though the concept of scale factor, the method of mode selection and the idea of consistent expression for the spatial distribution of load have been proposed in the authors' previous study [15], they will be further pursued in this paper in view of their different forms on a plate from those on a beam. This study investigates the problem of reconstructing distributed dynamic loads on a damped thin elastic plate with rectangular shape, uniform properties and simple boundary conditions. The objectives of the study are first, to introduce the concept of scale factor and the method of mode selection on a thin elastic plate, second, to develop a new theory of reconstructing distributed dynamic loads on the plate from its steady-state response, and finally, to formulate the criterion for the mode selection method and demonstrate its profits. The emphasis of the paper is placed on the theoretical analysis for load reconstruction, the criterion for mode selection, and the comparison between the mode selection method and the TSVD method.

In Sections 3.3 and 4.1, the method of truncated singular value decomposition (TSVD) and the method of mode selection are compared in theory and in simulations, respectively. With a fixed parameter noise level, the simulations show that the reconstruction is stable and robust when the latter method is applied, but may become unstable if the former one is used.

The rest of the paper is organized as follows. Section 2 first examines the dynamics of a thin elastic plate from a forward viewpoint, and then introduces the concept of scale factor and the method of mode selection from an inverse viewpoint. Section 3 begins with the description of consistent spatial expression for distributed dynamic loads, then develops the theory of load reconstruction subsequently, and introduces the difference between the method of mode selection and TSVD, and finally treats in detail the criterion of mode selection. In Section 4, numerical simulations are performed to disclose problems and to verify the theoretical results presented in Sections 2 and 3. Some conclusions are stated in Section 5.

2. Scale factor and mode selection

Consider a rectangular thin elastic plate, which is uniform, undamped and simply supported. The dynamic response of the plate yields the following dimensionless partial differential equation:

$$\frac{\pi^2(1+\lambda^2)^2}{4}\frac{\partial^2 Z(\xi,\eta,\tau)}{\partial\tau^2}+\Lambda Z(\xi,\eta,\tau)=p(\xi,\eta,\tau),$$
$$\Lambda\equiv\frac{\partial^4}{\partial\xi^4}+2\lambda^2\frac{\partial^4}{\partial\xi^2\partial\eta^2}+\lambda^4\frac{\partial^4}{\partial\eta^4},\quad D\equiv\frac{Eh^3}{12(1-\nu^2)},\tag{1}$$

where $\xi\equiv x/a$, $\eta\equiv y/b$ are the dimensionless spatial variables scaled by the corresponding side length of the plate, $\tau\equiv t/T$ is the dimensionless time scaled by $T\equiv 2a^2\sqrt{\rho h/D}/\pi(1+\lambda^2)$, $Z\equiv w/a$ is the dimensionless

translational displacement, $p \equiv a^3 f/D$ is the dimensionless distributed transverse excitation, and $\lambda \equiv a/b(\geqslant 1)$ is the aspect ratio, ρ is the density, E is the Young's modulus, v is the Poisson's ratio, and h is the thickness of the plate.

The modal analysis of the system gives the normalized modal functions and the corresponding natural frequencies

$$W_{mn}(\xi,\eta) = 2\,\sin(m\pi\xi)\,\sin(n\pi\eta), \quad \Omega_{mn} = 2\pi\frac{m^2+n^2\lambda^2}{1+\lambda^2}, \tag{2}$$

where $m,n \in \mathbb{N}$, and $\mathbb{N}$ is the set of all natural numbers.

In order to introduce the concept of scale factor and the method of mode selection, rearrange the natural frequencies in such an ascending order that

$$\Omega_k \equiv \Omega_{m_k n_k} = 2\pi\frac{m_k^2+n_k^2\lambda^2}{1+\lambda^2}, \quad \Omega_k \leqslant \Omega_{k+1}, \tag{3}$$

where $k \in \mathbb{N}$, and the corresponding normalized modal functions are denoted as

$$W_k(\xi,\eta) \equiv W_{m_k n_k}(\xi,\eta) = 2\,\sin(m_k\pi\xi)\,\sin(n_k\pi\eta). \tag{4}$$

With the modal transform $Z(\xi,\eta,\tau) = \sum_{k=1}^{\infty} W_k(\xi,\eta)q_k(\tau)$, the kth modal response corresponding to Eq. (1) becomes

$$\ddot{q}_k(\tau) + \Omega_k^2 q_k(\tau) = \frac{4}{\pi^2(1+\lambda^2)^2}p_k(\tau), \tag{5}$$

where

$$p_k(\tau) \equiv \int_0^1\int_0^1 W_k(\xi,\eta)p(\xi,\eta,\tau)\,\mathrm{d}\xi\,\mathrm{d}\eta, \quad k \in \mathbb{N}$$

the dot represents the derivative with respect to the dimensionless time τ, $q_k(\tau)$ is the modal coordinate, $p_k(\tau)$ is the general force, and $W_k(\xi,\eta)$ is the modal function, respectively.

Introducing modal damping into Eq. (5) gives

$$\ddot{q}_k(\tau) + 2\zeta_k\Omega_k\dot{q}_k(\tau) + \Omega_k^2 q_k(\tau) = \frac{4}{\pi^2(1+\lambda^2)^2}p_k(\tau), \quad k \in \mathbb{N}, \tag{6}$$

where ζ_k is the kth damping ratio. Hereinafter presented are the concept of scale factor and the method of mode selection.

2.1. Scale factor

If the transverse excitation is harmonic in the time domain and proportional to the jth mode shape in the spatial domain, namely,

$$p(\xi,\eta,\tau) = p_0 W_j(\xi,\eta)\,\mathrm{e}^{\mathrm{i}\Omega\tau}, \tag{7}$$

where p_0 is a real constant, then the general force and the corresponding steady-state response of the kth mode become

$$\begin{aligned} p_k(\tau) &= \delta_{jk}p_0\,\mathrm{e}^{\mathrm{i}\Omega\tau}, \\ q_k(\tau) &= \delta_{jk}\frac{4}{\pi^2(1+\lambda^2)^2}p_0\frac{1}{\Omega_k^2-\Omega^2+i2\zeta_k\Omega_k\Omega}\,\mathrm{e}^{\mathrm{i}\Omega\tau}, \end{aligned} \tag{8}$$

where $i = \sqrt{-1}$ and δ_{jk} is the Kronecker delta.

To examine the variance of the scale effect with both mode order k and excitation frequency Ω, it is useful to introduce the following *scale factor*

$$SF \equiv \frac{1}{\Omega_k^2 - \Omega^2 + \mathrm{i}2\zeta_k\Omega_k\Omega} = \frac{1}{\Omega^2}\frac{1}{\gamma^2 - 1 + \mathrm{i}2\zeta_k\gamma}, \tag{9}$$

where $\gamma \equiv \Omega_k/\Omega$. With help of this scale factor, the translational displacement of the steady-state response can be expressed as

$$Z(\xi,\eta,\tau) = \frac{4}{\pi^2(1+\lambda^2)^2} p_0 SF\, \mathrm{e}^{\mathrm{i}\Omega\tau} W_j(\xi,\eta). \tag{10}$$

The scale factor SF is a complex number with amplitude

$$|SF| \equiv \frac{1}{\Omega^2}\frac{1}{\sqrt{(\gamma^2-1)^2 + (2\zeta_k\gamma)^2}}, \tag{11}$$

which indicates that the scale effect comes from $c_s \equiv 1/\sqrt{(\gamma^2-1)^2 + (2\zeta_k\gamma)^2}$, where $\gamma \in (0,\infty)$. Fig. 1 shows the curve for c_s with fixed values $\zeta_k = 0.1$.

2.2. Mode selection

It is clear from Eq. (9) that the damped system is a low-pass filter in frequency domain. More important is the fact that the steady-state response of this system mainly depends on the combination of the frequency and the spatial distribution of the excitation. For example, given a harmonic excitation with a spatial distribution proportional to a specific mode, the steady-state response becomes significant if the excitation frequency is close to the natural frequency corresponding to this mode. Otherwise, the steady-state response is trivial. In a word, the steady-state response depends significantly on the difference between the excitation frequency and the natural frequencies corresponding to the modal components comprising the spatial distribution of the excitation, as well as on the excitation frequency.

The above observation leads to the first assertion of authors. That is, it is inherently a process of finite identification to reconstruct distributed dynamic loads on any continuum, if any modal expression is applied to describe the response. In fact, the difficulty in reconstructing the dynamic load of high frequency has been well acknowledged. Furthermore, the second point disclosed by the authors' study is that the reconstruction of distributed dynamic loads can only be made in a finite range, because the spatial modal components of the

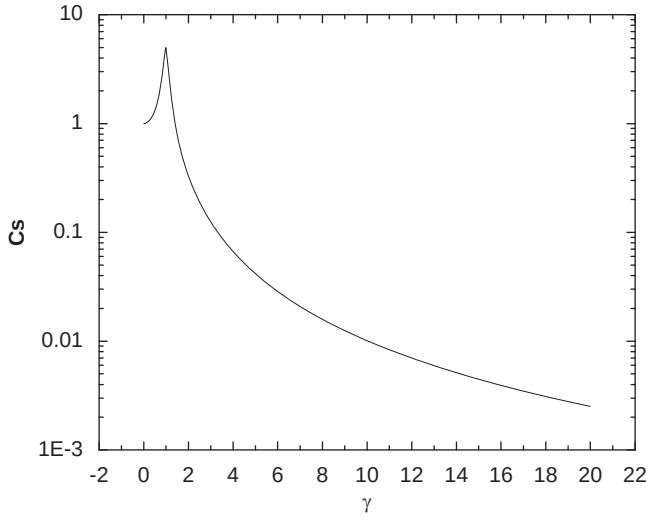

Fig. 1. Cs–Vs–γ.

excitation whose natural frequencies are distant from the excitation frequency have trivial attribution to the steady-state response and hence can hardly be reconstructed from the response.

The above discussion naturally leads to a *hypothesis* for the reconstruction of distributed dynamic loads as follows. Only a finite range of frequency and spatial modes of the distributed dynamic loads could be reconstructed from the response data, and there should be an optimal range for the load reconstruction when a specific level of measurement sensitivity and noise is known or estimated for a specific system. Furthermore, it should be remarked that this is analogous to the function of animal's ears, which means different animals have different ranges of sound perception due to their different structure of ears by nature.

Upon this hypothesis, a method named *mode selection* is proposed applying the concept of "scale factor" in Eq. (9) to determine an appropriate range for the load reconstruction. When the main frequencies of loads are obtained from the response, the scale factor SF of every mode can be determined, and only those modes, the amplitudes of whose corresponding scale factors divided by that of the maximum scale factor are larger than a threshold, will be chosen for the load reconstruction. Section 3.4 will derive a criterion to determine such a threshold. Meanwhile, the important role and effect of the scale factor has been demonstrated in the authors' previous study [15]. As the scale factor plays a similar role in the dynamic response of a thin elastic plate, it will not be described and demonstrated at length in this paper.

This method seems similar to the regularization method of discarding smaller singular values, namely TSVD. However, they are not the same concept in fact. When the regularization method TSVD is applied as an alternative method for mode selection, or as an alternative criterion in mode selection, the results are not as good as those with mode selection. Sections 3.3 and 4.1 will compare the method of mode selection with TSVD. Furthermore, it should be pointed out that, though the scale effect seems apparent in the forward problem and causes no trouble, it is the key point which results in ill-posedness and irreversibility in the inverse problem.

3. Reconstruction theory of distributed dynamic loads

3.1. Consistent spatial expression for distributed dynamic loads

In previous studies [11,14], modal functions or modified modal functions have been employed as the orthogonal base functions to describe the distributed dynamic loads, but these kinds of expressions conflict with the actual dynamic loads near the fixed boundaries of the structure. For instance, either the modal functions or the modified modal functions of a plate always tend to be zero near any fixed boundary, whereas the dynamic loads near the boundary may not vanish. Hence, with any linear combination of these base functions it is impossible to correctly describe the non-zero dynamic loads near any fixed boundary.

Therefore, it is proposed by the authors that some sort of consistent spatial expressions for distributed dynamic loads would be necessary to cope with this problem. In fact, there are a great variety of base functions for this purpose, such as many orthogonal polynomials. The authors' practice indicates that the double Legendre polynomials can offer a good example.

Provided that the distributed dynamic load on the plate is smoothly continuous in spatial dimensions, the spatial part of the load may be described by the expansion of a set of orthogonal base functions as

$$G(\xi,\eta)=\sum_{l} a_l \varphi_l(\xi,\eta), \tag{12}$$

where G is the spatial function of the load, φ_l is the lth orthogonal base function, and a_l is the corresponding lth coefficient. The set of base functions $\{\varphi_l\}$ can be orthonormal modal functions or orthonormal double Legendre polynomials expressed, respectively, as follows:

$$\varphi_l(\xi,\eta)\equiv W_l(\xi,\eta)=2\sin(m_l\pi\xi)\sin(n_l\pi\eta), \tag{13}$$

$$\varphi_l(\xi,\eta)\equiv P_{m_l}(\xi)P_{n_l}(\eta), \tag{14}$$

where the subscripts of the double Legendre polynomials are in accordance with those of the modal functions satisfying the condition described in Eq. (3).

3.2. Reconstruction theory

If the distributed dynamic load comprises N_p frequency components with different phase angles in time domain, it can be expressed as

$$p(\xi,\eta,\tau)=\sum_{r=1}^{N_p} G_r(\xi,\eta)\,\mathrm{e}^{\mathrm{i}(\hat{\Omega}_r\tau+\hat{\theta}_r)}. \tag{15}$$

Applying Eq. (15) into Eq. (6) leads to the general force and the corresponding steady-state response of the kth mode

$$p_k(\tau)=\sum_{r=1}^{N_p}\int_0^1\int_0^1 W_k(\xi,\eta)G_r(\xi,\eta)\,\mathrm{d}\xi\,\mathrm{d}\eta\,\mathrm{e}^{\mathrm{i}(\hat{\Omega}_r\tau+\hat{\theta}_r)}, \tag{16}$$

$$q_k(\tau)=\frac{4}{\pi^2(1+\lambda^2)^2}\sum_{r=1}^{N_p}\frac{1}{\Omega_k^2-\hat{\Omega}_r^2+i2\zeta_k\Omega_k\hat{\Omega}_r}\int_0^1\int_0^1 W_k(\xi,\eta)G_r(\xi,\eta)\,\mathrm{d}\xi\,\mathrm{d}\eta\,\mathrm{e}^{\mathrm{i}(\hat{\Omega}_r\tau+\hat{\theta}_r)}. \tag{17}$$

As shown in Eq. (9), the scale factor is defined as

$$SF(k,r)=\frac{1}{\Omega_k^2-\hat{\Omega}_r^2+i2\zeta_k\Omega_k\hat{\Omega}_r}. \tag{18}$$

To separate the spatial and temporal information from the steady-state response, it is helpful to introduce several abbreviation notations as follows

$$c_{kr}=\int_0^1\int_0^1 W_k(\xi,\eta)G_r(\xi,\eta)\,\mathrm{d}\xi\,\mathrm{d}\eta, \tag{19}$$

$$\psi_r(\xi,\eta)=\kappa\, e^{\mathrm{i}\hat{\theta}_r}\sum_{k=1}^{\infty} c_{kr}SF(k,r)W_k(\xi,\eta), \tag{20}$$

where $\kappa=4/\pi^2(1+\lambda^2)^2$, and ψ_r is a complex function of ξ and η. With help of the above notations, the translational displacement of the steady-state response of the plate can be written as

$$Z(\xi,\eta,\tau)=\sum_{r=1}^{N_p}\psi_r(\xi,\eta)\,\mathrm{e}^{\mathrm{i}\hat{\Omega}_r\tau}. \tag{21}$$

The process of reconstructing the distributed dynamic loads from the plate response begins with the measured steady-state translational displacements denoted as

$$Z(\xi_m,\eta_n,\tau_s),\quad m=1,\ldots,N_m,\ \ n=1,\ldots,N_n,\ \ s=1,\ldots,N_T, \tag{22}$$

where $N_m\times N_n$ is the number of points of the measurement-point rectangle on the plate, and N_T the number of data in the time dimension. Note that the distribution of the measurement points is not necessary to be a rectangle, but chosen in this study only for convenience. The frequency analysis gives the dominant circular frequencies and their corresponding real amplitudes and phase angles contained in the response data, namely

$$\hat{\Omega}_r,\quad \tilde{\psi}_r(\xi_m,\eta_n),\quad \tilde{\theta}_r(\xi_m,\eta_n), \tag{23}$$

where

$$r=1,\ldots,N_p,\quad m=1,\ldots,N_m,\quad n=1,\ldots,N_n,$$

N_p is the number of dominant frequencies, and $\hat{\Omega}_r$ is sorted so that $\hat{\Omega}_1<\cdots<\hat{\Omega}_{N_p}$.

Provided that the sets of Ω_k and ζ_k of modes are available, the scale factors SF can be calculated, and the necessary modes can be selected according to the criterion described in Section 3.4 and denoted as a set D_m. According to Eqs. (20) and (21), the combination of those real amplitudes and phase angles corresponding to

the rth dominant circular frequency $\hat{\Omega}_r$ can practically be given as the following truncated form:

$$\tilde{\psi}_r(\xi_m,\eta_n)\,\mathrm{e}^{\mathrm{i}\tilde{\theta}_r(\xi_m,\eta_n)} = \kappa\,\mathrm{e}^{\mathrm{i}\hat{\theta}_r}\sum_{k\in D_m} c_{kr}SF(k,r)W_k(\xi_m,\eta_n), \tag{24}$$

where $m=1,\ldots,N_m,\ n=1,\ldots,N_n$.

Eq. (24) may be an ill-posed problem for the solution of c_{kr} if the scale factors taken into account include excessively small ones. Hence, it may be necessary to employ the regularization approaches, such as TSVD or Tikhonov regularization [17,21,24]. However, it is demonstrated by theoretical discussion in Section 3.3 and numerical simulations in Section 4.1 that the employment of regularization may be avoided by applying the mode selection method together with its selection criterion, and that with these proposed approaches the reconstruction results can be actually improved. The solution of Eq. (24) for c_{kr} will be further pursued in Sections 3.3 and 3.4 by means of the method of mode selection and TSVD.

After c_{kr} is solved from Eq. (24), the last step is to solve Eq. (19) for $G_r(\xi,\eta)$. Eq. (19) can be regarded as a mapping A from the space of all kinds of $G_r(\xi,\eta)$, denoted as U, to the space of all $W_k(\xi,\eta)$, denoted as V. That is, $A: U\to V$. Hence, Eq. (19) can be solved for $G_r(\xi,\eta)$ by using the projection method [25] as follows.

Let U_L be an L-dimensional subspace of U with a series of orthogonal base functions $\{\varphi_l(\xi,\eta)\}$ with respect to a given inner product, V_K be a K-dimensional subspace of V with a series of orthogonal base functions $\{W_k(\xi,\eta)\}$ having the inner product defined by $\langle W_i,W_j\rangle=\int_0^1\int_0^1 W_i(\xi,\eta)W_j(\xi,\eta)\,d\xi\,d\eta$, and the following relations hold

$$U_L\subset U_{L+1}\subset\cdots\subset U,\quad V_K\subset V_{K+1}\subset\cdots\subset V. \tag{25}$$

The definition of a projection operator $Q_K: V\to V_K$ enables one to establish an approximate projection

$$Q_KA|_{U_L}: U_L\to V_K. \tag{26}$$

Therefore, Eq. (19) as an approximate projection (26) can easily be recast as the following matrix equation:

$$\mathbf{Aa}=\mathbf{c}, \tag{27}$$

where

$$\mathbf{A}\equiv\left[\int_0^1\int_0^1 W_k(\xi,\eta)\varphi_l(\xi,\eta)\,\mathrm{d}\xi\,\mathrm{d}\eta\right]_{K\times L},\quad \mathbf{c}\equiv\{c_{kr}\}_{K\times 1},$$

and $\mathbf{a}$ is the vector of expansion coefficients in Eq. (12). Solving Eq. (27) for $\mathbf{a}$, one at last reaches the spatial distribution function

$$\mathbf{G}_r(\xi,\eta)=\mathbf{a}^{\mathrm{T}}\boldsymbol{\varphi}(\xi,\eta). \tag{28}$$

3.3. TSVD and mode selection

This subsection discusses the solution of Eq. (24) for c_{kr} in detail, and thus introduces the comparison between the methods of TSVD and mode selection.

Suppose that the mode set D_m is known, and denote the number of the modes included in the set as N_D. Now rewrite Eq. (24) concisely in a matrix form

$$\boldsymbol{\psi}=\mathbf{Hc}', \tag{29}$$

where $\mathbf{c}'=\mathbf{c}\mathrm{e}^{\mathrm{i}\hat{\theta}_r}$, $\mathbf{H}=\mathbf{WSF}$, $\mathbf{W}=[W_k(\xi_m,\eta_n)]_{N_{\xi\eta}\times N_D}$, $\mathbf{SF}=[SF(k,r)]_{N_D\times N_D}$ is a complex diagonal matrix, $\boldsymbol{\psi}=\{\tilde{\psi}_r(\xi_m,\eta_n)\,\mathrm{e}^{\mathrm{i}\tilde{\theta}_r(\xi_m,\eta_n)}\}_{N_{\xi\eta}\times 1}/\kappa$ is a complex vector, $\mathbf{c}=\{c_{kr}\}_{N_D\times 1}$ is a real vector, $\hat{\theta}_r$ is the phase angle, and $N_{\xi\eta}=N_m\times N_n$. Note that in this equation both the vector $\mathbf{c}$ and the phase angle $\hat{\theta}_r$ are unknown.

To solve the above equation for $\mathbf{c}'$, one has at least two methods on hand. That is, the pseudoinverse method and the TSVD method.

By means of the pseudoinverse method, one can obtain the least squared solution of Eq. (29):

$$\mathbf{c}'=\mathbf{H}^{+}\boldsymbol{\psi}, \tag{30}$$

where the superscript plus denotes the Moore–Penrose pseudoinverse, and $\mathbf{H}$ is formed by virtue of mode selection, of which the selection criterion is addressed in Section 3.4.

On the other hand, the method TSVD can be employed in two ways. One is direct, named as DTSVD. The other is indirect, named as IDTSVD. With DTSVD, the truncated Eq. (29) is not based on the mode selection but on the estimation of enough modes for consideration, and then it is solved by TSVD. In simulations in Section 4, the modes under consideration with DTSVD are the first 20 modes with the lowest natural frequencies. This method fails to work in most cases during numerous simulations, but in the first case study in this manuscript it shows acceptable result, and they are displayed just to show its instability.

With IDTSVD, the truncated Eq. (29) is first established from the same estimation of enough modes for consideration as with DTSVD, and then the regularization parameter $k(T)$ may be obtained from Eq. (29) with TSVD. However, this parameter is used as a criterion for mode selection to reform Eq. (29), and the equation is finally solved with the pseudoinverse method.

The final solution for the real vector $\mathbf{c}$ can be found by the method of nonlinear optimization, which is to find an optimum $\hat{\theta}_r$ with the objective minimizing the norm of the imaginary part of $\mathbf{c}'\,\mathrm{e}^{-\mathrm{i}\hat{\theta}_r}$. It has two optimal values for $\hat{\theta}_r$ in a range of $[0,2\pi)$, but one can assume $\hat{\theta}_r \in [0,\pi)$ in Eq. (15) without loss of generality to guarantee the unique optimum. Once the value of $\hat{\theta}_r$ is obtained, the vector $\mathbf{c}$ reads

$$\mathbf{c} = \mathrm{Re}(\mathbf{c}'\mathrm{e}^{-\mathrm{i}\hat{\theta}_r}). \tag{31}$$

3.4. Criterion for mode selection

In the above subsection, a criterion for mode selection is just touched upon. This subsection is devoted to the formulation of this criterion with the aim of determining the mode set D_m in Eq. (24) for the mode selection method.

Eq. (29) is the matrix form of Eq. (24). Considering the practical errors involved in the formulation of Eq. (29), the equation becomes a linear least squares problem

$$\min_{\mathbf{c}'\in\mathbb{C}^{N_D}} ||\mathbf{H}\mathbf{c}' - \boldsymbol{\psi}||_2, \tag{32}$$

where $\mathbf{H} \in \mathbb{C}_{N_D}^{N_{\xi\eta}\times N_D}$, $N_D < N_{\xi\eta}$, $\boldsymbol{\psi} \in \mathbb{C}^{N_{\xi\eta}}$, $\mathbb{C}$ is the set of all complex numbers, and $||\cdot||_2$ denotes the l^2-norm for vectors or the induced spectral norm for matrices, similarly hereafter.

The proposed criterion is derived from the Rice condition number of the solution to the above problem. The 2-norm relative condition number [26] of the solution to problem (32) may be expressed as

$$c_2(\mathbf{H},\boldsymbol{\psi};\mathbf{c}') = ||\mathbf{H}^+||_2\sqrt{||\mathbf{H}||_2^2(||\mathbf{c}'||_2^2 + (||\mathbf{H}^+||_2||\mathbf{r}||_2)^2) + ||\boldsymbol{\psi}||_2^2}/||\mathbf{c}'||_2, \tag{33}$$

where $\mathbf{r} = \boldsymbol{\psi} - \mathbf{H}\mathbf{c}'$, and the following inequality holds as a first-order approximation

$$||\Delta\mathbf{c}'||_2/||\mathbf{c}'||_2 \leqslant c_2(\mathbf{H},\boldsymbol{\psi};\mathbf{c}')||(||\Delta\mathbf{H}||_2/||\mathbf{H}||_2, ||\Delta\boldsymbol{\psi}||_2/||\boldsymbol{\psi}||_2)^{\mathrm{T}}||_2. \tag{34}$$

The modal matrix $\mathbf{W}$ is of full column rank N_B provided that the number of measurement points is large enough. Thus it holds that $\mathbf{H}^+ = \mathbf{S}\mathbf{F}^{-1}\mathbf{W}^+$. In general, $||\boldsymbol{\psi}||_2 \approx ||\mathbf{H}\mathbf{c}'||_2$. Then, Eq. (33) becomes

$$\begin{aligned} c_2(\mathbf{H},\boldsymbol{\psi};\mathbf{c}') &\approx ||\mathbf{H}^+||_2||\mathbf{H}||_2\sqrt{2 + (||\mathbf{H}^+||_2||\mathbf{r}||_2/||\mathbf{c}'||_2)^2} \\ &\leqslant ||\mathbf{W}^+||_2||\mathbf{W}||_2||\mathbf{S}\mathbf{F}^{-1}||_2||\mathbf{S}\mathbf{F}||_2\sqrt{2 + (||\mathbf{S}\mathbf{F}^{-1}||_2||\mathbf{W}^+||_2||\mathbf{r}||_2/||\mathbf{c}'||_2)^2}. \end{aligned} \tag{35}$$

It requires in mode selection that $\sigma_{\min}(\mathbf{S}\mathbf{F})/\sigma_{\max}(\mathbf{S}\mathbf{F}) \geqslant \varepsilon_{SF}$, namely, $||\mathbf{S}\mathbf{F}^{-1}||_2||\mathbf{S}\mathbf{F}||_2 \leqslant 1/\varepsilon_{SF}$, where $\sigma_{\min}$ and $\sigma_{\max}$ represent the smallest singular value and the largest one, respectively. Hence, the above relation becomes

$$c_2(\mathbf{H},\boldsymbol{\psi};\mathbf{c}') \leqslant \frac{||\mathbf{W}^+||_2||\mathbf{W}||_2}{\varepsilon_{SF}}\sqrt{2 + \left(\frac{||\mathbf{W}^+||_2||\mathbf{r}||_2}{\varepsilon_{SF}||\mathbf{S}\mathbf{F}||_2||\mathbf{c}'||_2}\right)^2}. \tag{36}$$

Suppose that the relative errors $||\Delta\mathbf{H}||_2/||\mathbf{H}||_2$ and $||\Delta\boldsymbol{\psi}||_2/||\boldsymbol{\psi}||_2$ are known or estimated and that one expects to control the relative error of reconstructed vector $\mathbf{c}$, namely, $||\Delta\mathbf{c}'||_2/||\mathbf{c}'||_2$, under the error control

parameter e_c, then the permitted least upper bound for the 2-norm relative condition number sup $c_2(\mathbf{H},\boldsymbol{\psi};\mathbf{c}')$ can be obtained from Eq. (34) by imposing that

$$\sup c_2(\mathbf{H},\boldsymbol{\psi};\mathbf{c}') \leqslant e_c/||(||\Delta\mathbf{H}||_2/||\mathbf{H}||_2, ||\Delta\boldsymbol{\psi}||_2/||\boldsymbol{\psi}||_2)^{\mathrm{T}}||_2. \tag{37}$$

Finally, the criterion threshold ε_{SF} is obtained from Eq. (36) by requiring that

$$\frac{||\mathbf{W}^+||_2||\mathbf{W}||_2}{\varepsilon_{SF}}\sqrt{2+\left(\frac{||\mathbf{W}^+||_2||\mathbf{r}||_2}{\varepsilon_{SF}||\mathbf{SF}||_2||\mathbf{c}'||_2}\right)^2} \leqslant \sup\ c_2(\mathbf{H},\boldsymbol{\psi};\mathbf{c}'), \tag{38}$$

if $||\mathbf{r}||_2$ and $||\mathbf{c}'||_2$ can be estimated. Consequently, the modes will be selected so as to satisfy the following inequality:

$$|SF(k,r)| \Big/ \max_{n\in D}(|\mathrm{SF}(n,r)|) \geqslant \varepsilon_{SF}(r), \quad k \in D,\ \ r = 1 \ldots N_p \tag{39}$$

where D is a set including enough modes for consideration, and the mode set D_m is finally determined.

4. Case studies

All case studies in this section deal with a dynamic system described by Eq. (6) whose parameters include the aspect ratio $\lambda = 7/3$ and the damping ratios $\zeta_k = 0.2 + 0.3(k-1)/39$ when $k = 1,\ldots,40$ and $\zeta_k = \infty$ when $k = 41,\ldots,\infty$. The dimensionless system results from a rectangular thin elastic plate, which is uniform, damped and simply supported.

In the following numerical simulations, the discrete dimensionless translational displacements of the system are sampled from the analytical solution by the mode superposition principle, and only steady-state responses are under consideration. Modes of up to 40 orders are used to simulate the response, but only the modes of up to 20 orders are applied to reconstruct the load. The total dimensionless time length is $T = 10$, the sampling rate is $\Delta\tau = 0.01$, and the distribution of measurement position is $(\xi_i,\eta_j) = (i/9, j/9)$ with $i,j = 1,\ldots,8$.

Uniformly distributed random noises are applied to the displacements, natural frequencies, mode shapes, and damping ratios. The noise applied to the dimensionless displacements is an additive noise of the maximum displacement multiplied by a noise factor, whose upper bound is denoted as α_Z. The noise to the dimensionless natural frequencies is an additive noise of the lowest dimensionless natural frequency multiplied by a noise factor, whose upper bound is denoted as α_O. The noise to the dimensionless orthonormal mode shapes is a multiplicative noise, the upper bound of whose noise factor is denoted as α_W. And the noise to the damping ratios is a multiplicative noise, the upper bound of whose noise factor is denoted as α_ς. The signal-to-noise ratios of the above resulting noisy data are denoted as SNR_Z, SNR_O, SNR_W and SNR_ς, respectively. However, no noise is applied to the dimensionless orthonormal mode shapes when they are used as orthogonal base functions in the projection method in Section 3.2.

Furthermore, in all the following results, the relative errors are defined as the absolute errors divided by the maximum value of the original data.

4.1. Comparisons among methods DTSVD, IDTSVD and mode selection

The first case study serves to compare the three methods mentioned in Section 3.3. The system is subject to the harmonic excitation $p(\xi,\eta,\tau) = W_3(\xi,\eta)\cos(\hat{\Omega}\tau + \hat{\theta})$, where $\hat{\Omega} = \Omega_2 + 0.5\Omega_1$ and $\hat{\theta} = \pi/3$. The relevant noise levels are $\alpha_O = 0.01$ and $\alpha_Z = \alpha_W = \alpha_\varsigma = 0.1$. Fig. 2(a) shows the spatial distribution of the excitation.

As two methods for choosing regularization parameter, namely, L-curve criterion and generalized cross-validation (GCV), are available for the reconstruction, they both are considered for illustration. Four simulations are displayed for each of methods DTSVD and IDTSVD, two for method GCV and the other two for L-curve criterion. There are 10 simulations presented in this case study. Simulations 1-1 to 1-4 are for method DTSVD, among which simulations 1-1 and 1-2 are for GCV and simulations 1-3 and 1-4 are for L-curve. Simulations 1-5 to 1-8 are for method IDTSVD, among which simulations 1-5 and 1-6 are for GCV and simulations 1-7 and 1-8 are for L-curve. Simulations 1-9 and 1-10 are for the mode selection method with

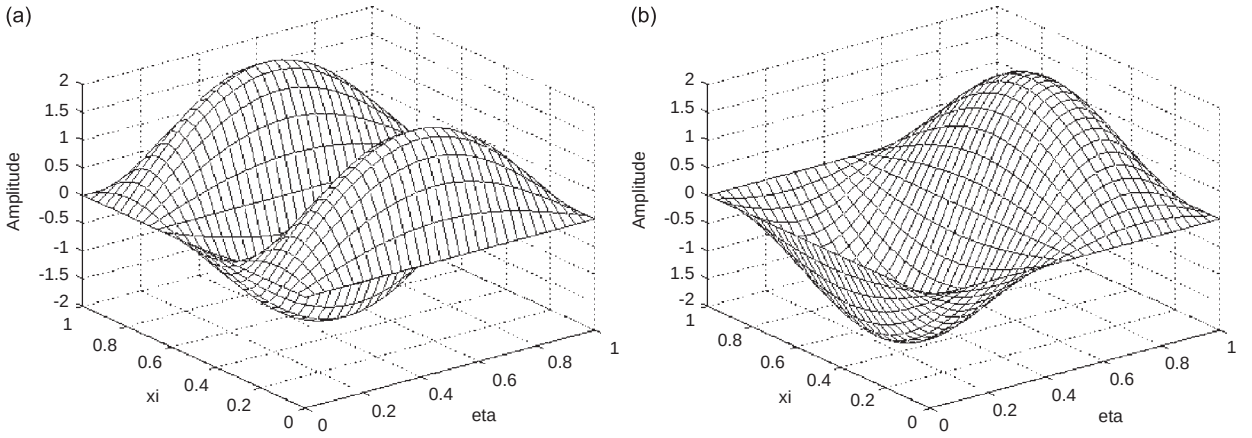

Fig. 2. Original load distributions: (a) for Case 1 and for the first frequency component in Case 3 and (b) for the second frequency component in Case 3.

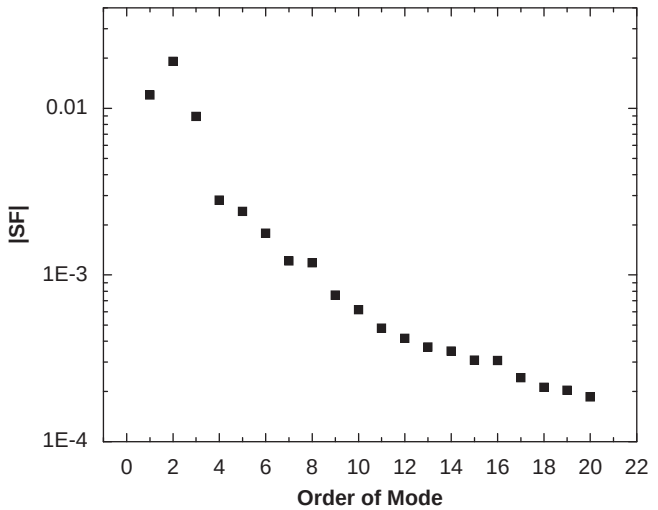

Fig. 3. Scale factors for Cases 1, 2, and 5.

error control parameter $e_c = 1$, and Fig. 3 shows the variation of the scale factors SF with respect to the order of mode.

Table 1 presents the signal-to-noise ratios for the resulting simulation data and Table 2 shows all the relevant reconstruction results except the spatial error distribution. The spatial error distributions of reconstructed loads are illustrated in Figs. 4–8.

Simulations 1-1, 1-4, 1-6 and 1-7 have rather good results of load reconstruction, while simulations 1-2, 1-3, 1-5 and 1-8 have poor levels of reconstruction error, respectively. The latter poor results seldom appear, but they did appear. The difference between the good ones and the poor ones can be distinguished from the values of the regularization parameter $k(T)$ in Table 2 and their reconstruction error levels in Figs. 4–7. The application of the two methods, GCV and L-curve criterion, on the authors' study are unstable, even when the same case, with different but the same level noise, is dealt with. On the other hand, the proposed method of mode selection is rather stable, which may be concluded from the extreme reconstruction situations 1-9 and 1-10 whose reconstruction errors are displayed in Fig. 8.

Consequently, the load reconstruction is unstable with methods DTSVD and IDTSVD, probably because unstable regularization-parameter selection happens when errors are under consideration, which maybe is an

Table 1
Signal-to-noise ratios for Case 1.

Method	Simulation	SNR_Z	SNR_O	SNR_W	SNR_ζ
DTSVD					
GCV	1-1	18.1466	55.9526	24.5842	8.7279
	1-2	18.1305	54.4237	24.6654	8.0286
L-curve	1-3	18.1244	56.6303	24.9511	10.1629
	1-4	18.1179	54.8658	24.6910	8.0930
IDTSVD					
GCV	1-5	18.1343	54.6461	24.5243	9.8508
	1-6	18.1269	54.8295	24.4994	10.2294
L-curve	1-7	18.1317	54.6590	24.7402	8.7936
	1-8	18.1269	54.8295	24.4994	10.2294
Mode selection	1-9	18.1454	54.3879	24.7872	10.6104
	1-10	18.1145	56.5100	24.7003	7.9727

Table 2
Relevant reconstruction results for Case 1.

Method	Simulation	$k(T)\|\varepsilon_{SF}$	D_m	$\Delta\hat{\Omega}$	$\Delta\hat{\theta}$ (rad)
DTSVD					
GCV	1-1	$k(T)=3$	–	−0.0137	0.0445
	1-2	$k(T)=18$	–	−0.0039	−0.2591
L-curve	1-3	$k(T)=15$	–	−0.0145	−0.1365
	1-4	$k(T)=6$	–	0.0047	0.0371
IDTSVD					
GCV	1-5	$k(T)=10$	1…10	0.0047	−0.0223
	1-6	$k(T)=3$	1…3	0.0008	−0.0258
L-curve	1-7	$k(T)=6$	1…6	0.0158	0.0240
	1-8	$k(T)=10$	1…10	0.0008	−0.0406
Mode selection	1-9	$\varepsilon_{SF}=0.1362$	1…4	0.0100	0.0172
	1-10	$\varepsilon_{SF}=0.0930$	1…6	0.0200	−0.0232

intrinsic drawback in method TSVD. Meanwhile, the reconstruction is rather stable with the mode selection method together with the proposed criterion.

4.2. Influence of the selection criterion on mode selection method

The second case study is devoted to illustrating the influence of error control parameter e_c on the method of mode selection. The system is subject to a harmonic excitation $p(\xi,\eta,\tau)=(\eta-\xi^2)\cos(\hat{\Omega}\tau+\hat{\theta})$, where $\hat{\Omega}=\Omega_2+0.5\Omega_1$ and $\hat{\theta}=\pi/3$. The relevant noise levels are $\alpha_O=0.001$ and $\alpha_Z=\alpha_W=\alpha_\zeta=0.01$. Fig. 9(a) shows the spatial distribution of the excitation.

This case study includes simulations 2-1 to 2-4. Table 3 presents the signal-to-noise ratios for the resulting simulation data and all the relevant reconstruction results except the spatial error distribution. The zero value of ε_{SF} in simulation 2-4 in Table 3 indicates that the selected mode range is beyond the 20 modes under consideration. Fig. 3 shows the variation of the scale factors SF with respect to the order of mode. The spatial error distributions of reconstructed loads are illustrated in Fig. 10.

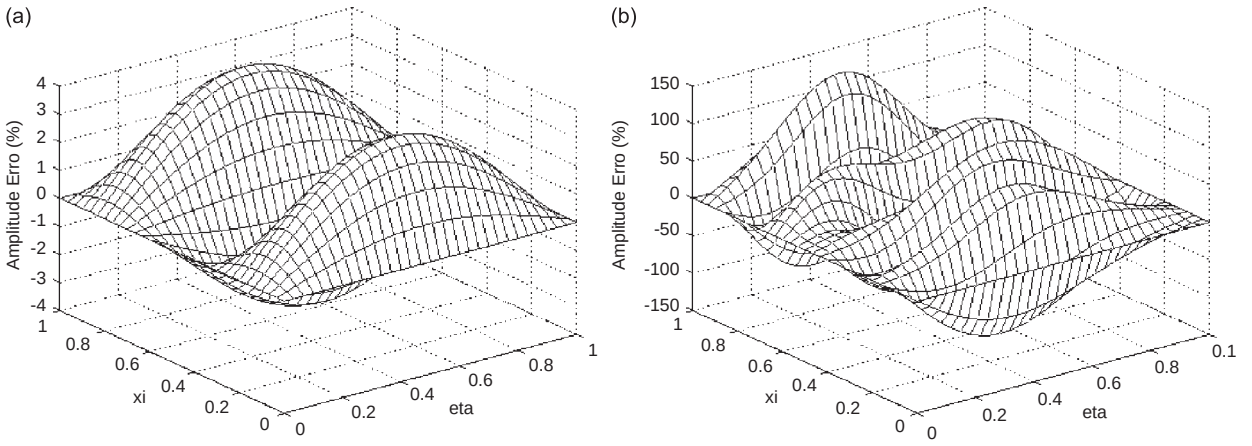

Fig. 4. Error distributions for Case 1 with method DTSVD and GCV: (a) for simulation 1–1 and (b) for simulation 1–2.

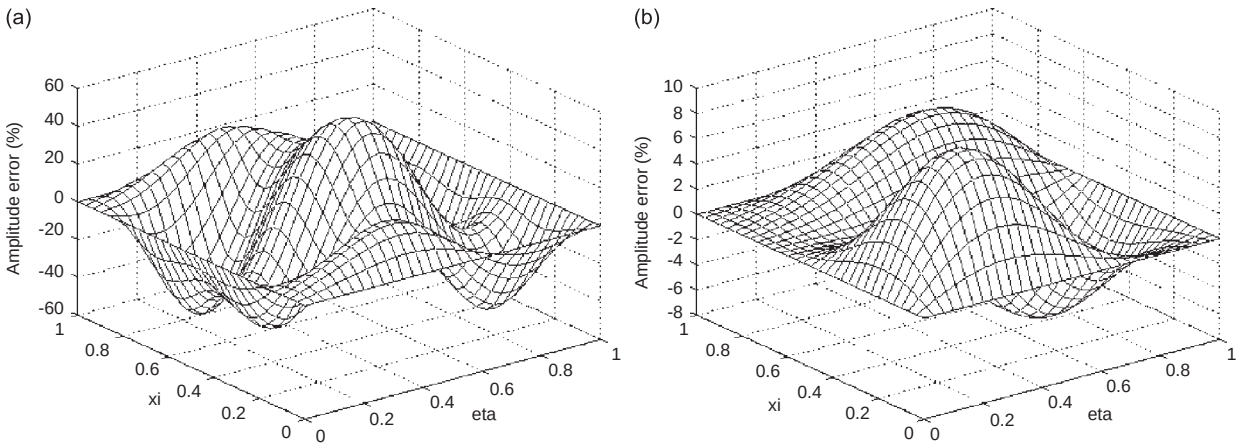

Fig. 5. Error distributions for Case 1 with method DTSVD and L-curve: (a) for simulation 1–3 and (b) for simulation 1–4.

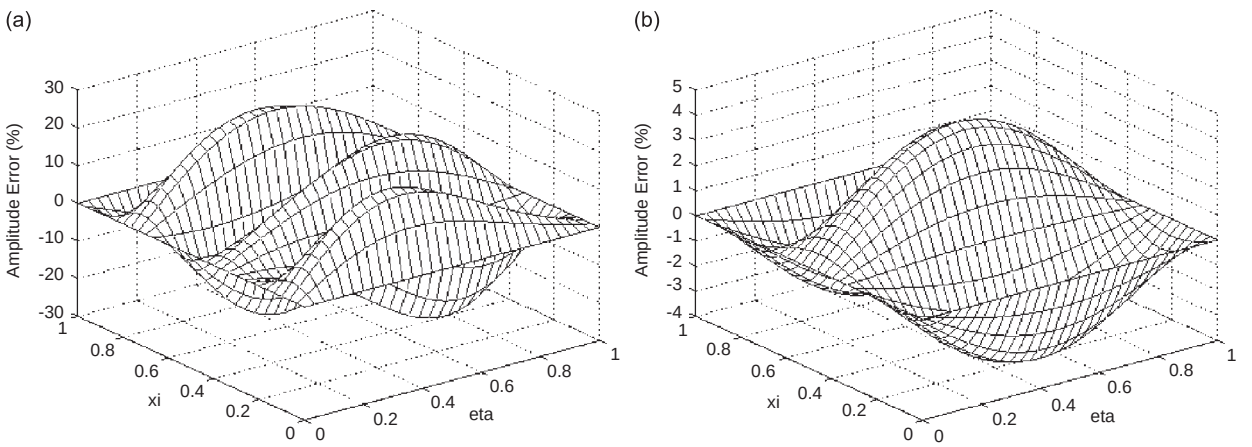

Fig. 6. Error distributions for Case 1 with method IDTSVD and GCV: (a) for simulation 1–5 and (b) for simulation 1–6.

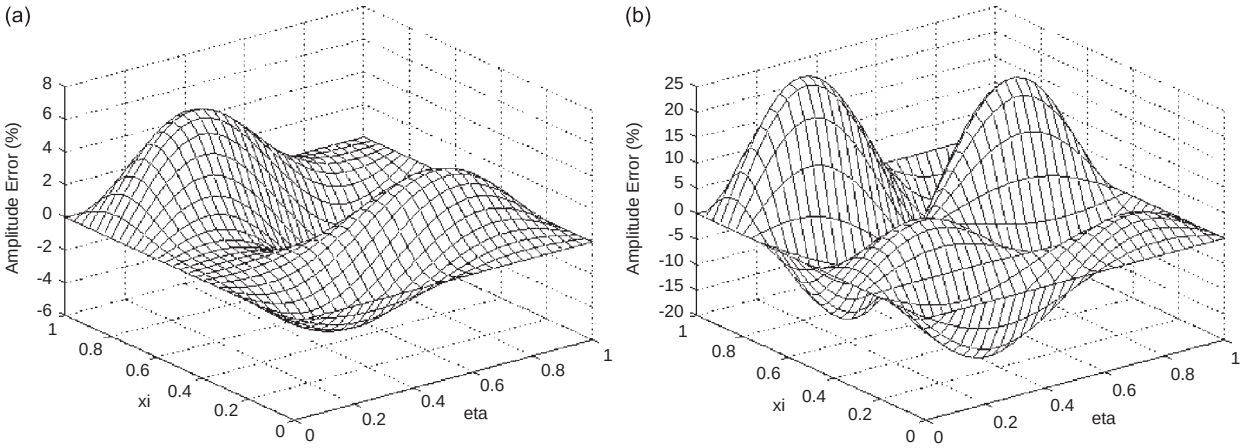

Fig. 7. Error distributions for Case 1 with method IDTSVD and L-curve: (a) for simulation 1–7 and (b) for simulation 1–8.

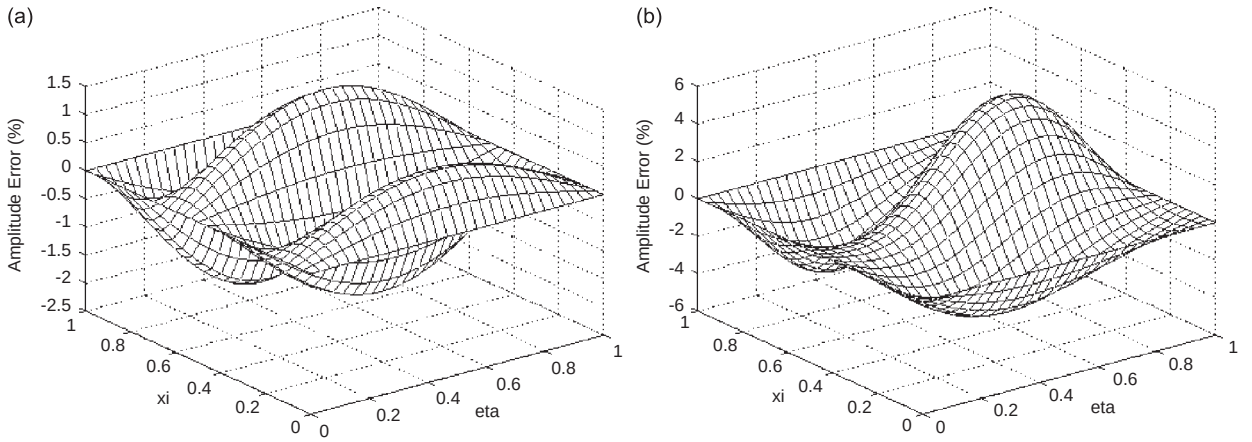

Fig. 8. Error distributions for Case 1 with method mode selection and selection criterion: (a) for simulation 1–9 and (b) for simulation 1–10.

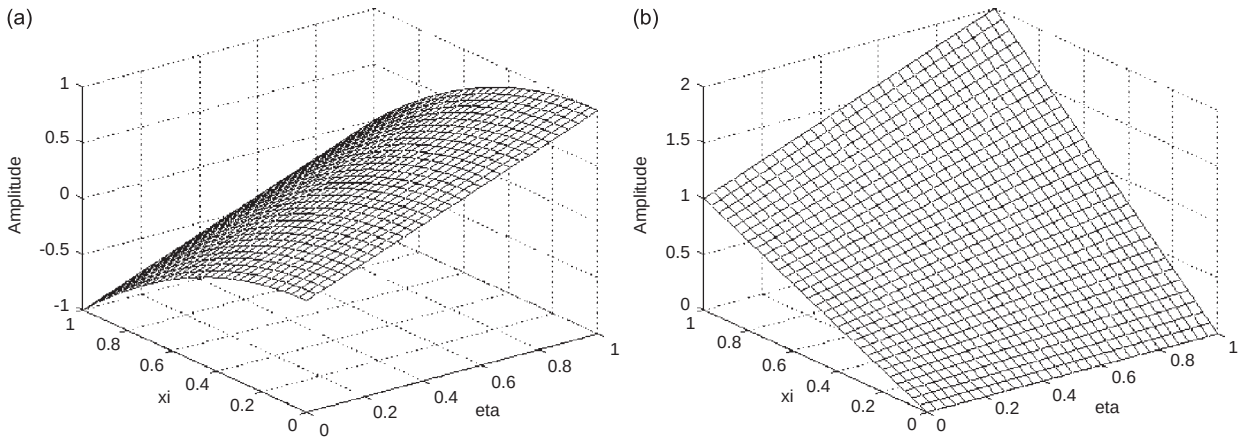

Fig. 9. Original load distributions: (a) for Case 2 and for the first frequency component in Case 7 and (b) for the second frequency component in Case 7.

Table 3
Signal-to-noise ratios and relevant reconstruction results for Case 2.

–	Simulation 2-1	Simulation 2-2	Simulation 2-3	Simulation 2-4
	$e_c = 0.1$	$e_c = 0.5$	$e_c = 1$	$e_c = 5$
SNR_Z	35.6229	35.6057	35.6198	35.6091
SNR_O	74.6590	76.5100	74.9445	74.8658
SNR_W	44.7402	44.7003	44.7072	44.6910
SNR_ζ	28.7936	27.9727	27.5305	28.0930
$\varepsilon_{\mathrm{SF}}$	0.1240	0.0179	0.0133	0
D_m	1…5	1…14	1…16	1…20
$\Delta\hat{\Omega}$	0.0010	−0.0021	−0.0026	−0.0015
$\Delta\hat{\theta}$ (rad)	−0.0015	−0.0027	−0.0009	0.0011

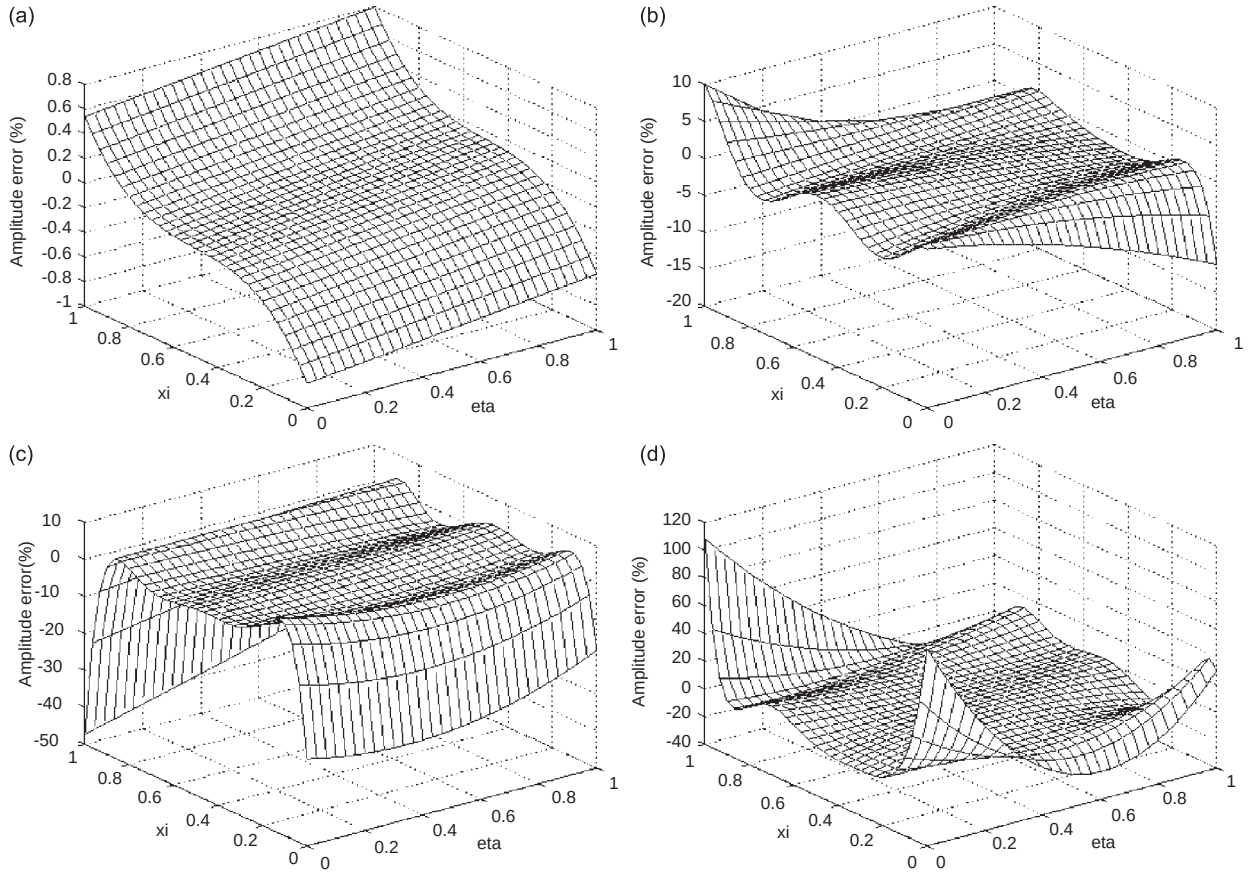

Fig. 10. Error distributions for Case 2 with method Mode Selection and varying parameter e_c: (a) for simulation 2–1, $e_c = 0.1$; (b) for simulation 2–2, $e_c = 0.5$; (c) for simulation 2–3, $e_c = 1$; (d) for simulation 2–4, $e_c = 5$.

From Fig. 10, it is clear that smaller error expectation, namely smaller error control parameter e_c, results in narrower selected mode range and better reconstruction accuracy compared to larger error control parameter e_c, only if it does not exceed the critical value which is not yet known. From the other point of view, larger error expectation, or larger error control parameter e_c, results in broader selected mode range, which means broader reconstruction domain, though reconstruction accuracy will decrease. Therefore, the mode selection

method may be applied to make a balance between reconstruction range and accuracy, whereas the method of TSVD fails to do so. It is also disclosed by the simulations that the criterion needs further improvement, because the reconstruction is much more accurate than the expectation given by the error control parameter e_c.

4.3. More complex case studies

The following case studies show the effect of the mode selection method in different complex situations. The third case and the fourth case are presented for complex situations of mode-composed spatial distribution, while the fifth case through the seventh case are illustrated for situations of polynomial-composed spatial distribution.

In the third case, the system is subject to a compound excitation with two harmonic components $p(\xi,\eta,\tau)=W_3(\xi,\eta)\cos(\hat{\Omega}_1\tau+\hat{\theta}_1)-W_5(\xi,\eta)\cos(\hat{\Omega}_2\tau+\hat{\theta}_2)$. In the fourth case, the excitation is of a complex form of $p(\xi,\eta,\tau)=\sum_{i=1,3}f_iW_i(\xi,\eta)\cos(\hat{\Omega}_1\tau+\hat{\theta}_1)+\sum_{j=2,5}g_jW_j(\xi,\eta)\cos(\hat{\Omega}_2\tau+\hat{\theta}_2)$, where $f_1=g_2=g_5=1$, $f_3=-1$.

In the fifth case, the system is excited by a harmonic load with uniform spatial distribution $p(\xi,\eta,\tau)=\cos(\hat{\Omega}_1\tau+\hat{\theta}_1)$. In the sixth case, the excitation is a compound load with two harmonic components $p(\xi,\eta,\tau)=\cos(\hat{\Omega}_1\tau+\hat{\theta}_1)-\xi^2\cos(\hat{\Omega}_2\tau+\hat{\theta}_2)$. In the seventh case, the system is under a compound load with complex spatial distribution $p(\xi,\eta,\tau)=(\eta-\xi^2)\cos(\hat{\Omega}_1\tau+\hat{\theta}_1)+(\xi+\xi\eta)\cos(\hat{\Omega}_2\tau+\hat{\theta}_2)$.

Table 4 presents the frequencies $\hat{\Omega}_1,\hat{\Omega}_2$, phase angles $\hat{\theta}_1,\hat{\theta}_2$, relevant noise levels $\alpha_Z,\alpha_O,\alpha_W,\alpha_\zeta$, signal-to-noise ratios $\mathrm{SNR}_Z,\mathrm{SNR}_O,\mathrm{SNR}_W,\mathrm{SNR}_\zeta$, mode selection threshold ε_{SF}, mode range D_m, errors between reconstructed and original frequencies $\Delta\hat{\Omega}_1,\Delta\hat{\Omega}_2$, and errors between reconstructed and original phase angles $\Delta\hat{\theta}_1,\Delta\hat{\theta}_2$, of all the cases addressed in this subsection. Fig. 3 shows for Case 5 the variation of the scale factors SF with respect to the order of mode, while Fig. 11 shows for Cases 3, 4, 6, and 7 the variation of the scale factors SF with respect to the order of mode.

The original load distributions are shown in Fig. 2 for Case 3, in Fig. 12 for Case 4, in Fig. 13 for Cases 5 and 6, and in Fig. 9 for Case 7, respectively, and their corresponding spatial error distributions of reconstructed loads are illustrated in Figs. 14–18.

Table 4
Reconstruction parameters and relevant results for Cases 3–7.

–	Case 3 $e_c=1$	Case 4 $e_c=1$	Case 5 $e_c=1$	Case 6 $e_c=0.1$	Case 7 $e_c=0.5$
$\hat{\Omega}_1$	$\Omega 2+0.5\Omega_1$	$\Omega 2+0.5\Omega_1$	$\Omega 2+0.5\Omega_1$	$\Omega 2+0.5\Omega_1$	$\Omega 2+0.5\Omega_1$
$\hat{\Omega}_2$	$\Omega 5+0.8\Omega_1$	$\Omega 5+0.8\Omega_1$	–	$\Omega 5+0.8\Omega_1$	$\Omega 5+0.8\Omega_1$
$\hat{\theta}_1$	$\pi/3$	$\pi/3$	$\pi/3$	$\pi/3$	$\pi/3$
$\hat{\theta}_2$	$3\pi/4$	$3\pi/4$	–	$3\pi/4$	$3\pi/4$
α_O	0.01	0.01	0.01	0.001	0.001
α_Z, α_W, α_ζ	0.1	0.1	0.1	0.01	0.01
SNR_Z	16.5172	16.6665	16.2398	36.0782	34.8004
SNR_O	54.6461	54.5454	56.6537	75.4663	75.3568
SNR_W	24.5243	24.7515	24.8062	44.7637	44.6863
SNR_ζ	9.8508	8.6759	7.3533	28.3082	29.7049
$\varepsilon_{\mathrm{SF}}(\hat{\Omega}_1)$	0.1275	0.1808	0.1584	0.3953	0.0303
$D_m(\hat{\Omega}_1)$	1…5	1…3	1…3	1…3	1…10
$\Delta\hat{\Omega}_1$	0.0059	−0.0068	0.0130	0.0080	−0.0028
$\Delta\hat{\theta}_1$ (rad)	0.0070	0.0336	−0.0261	0.0014	0.0014
$\varepsilon_{\mathrm{SF}}(\hat{\Omega}_2)$	0.1538	0.1806	–	0.4049	0
$D_m(\hat{\Omega}_2)$	1…10	1…10	–	1…8	1…20
$\Delta\hat{\Omega}_2$	0.0449	0.0294	–	–0.0350	0.0052
$\Delta\hat{\theta}_2$ (rad)	−0.0066	−0.0154	–	−0.0240	–0.0002

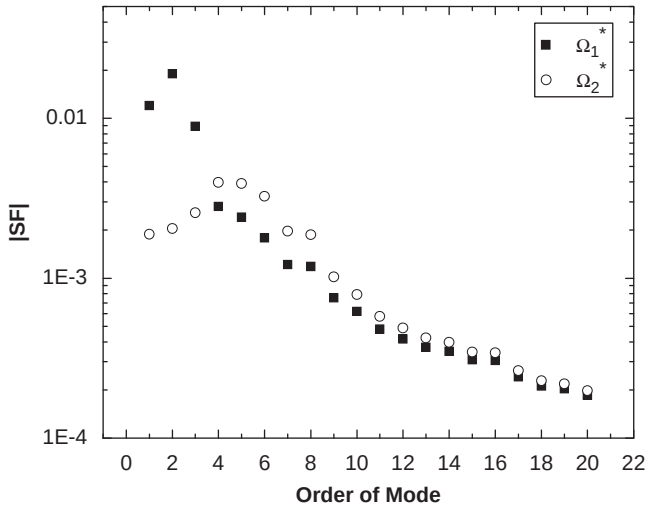

Fig. 11. Scale factors for Cases 3, 4, 6, and 7.

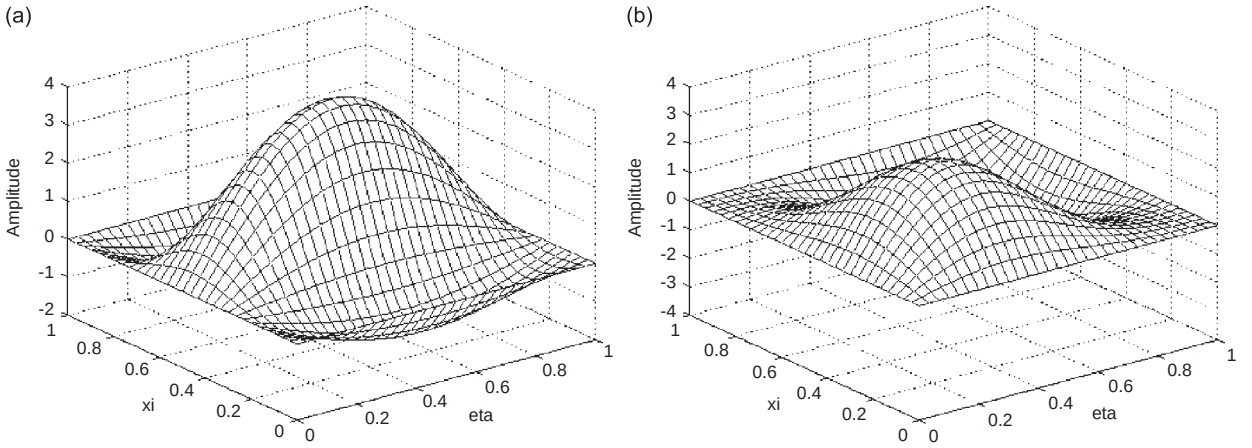

Fig. 12. Original load distributions for Case 4: (a) for the first frequency component and (b) for the second frequency component.

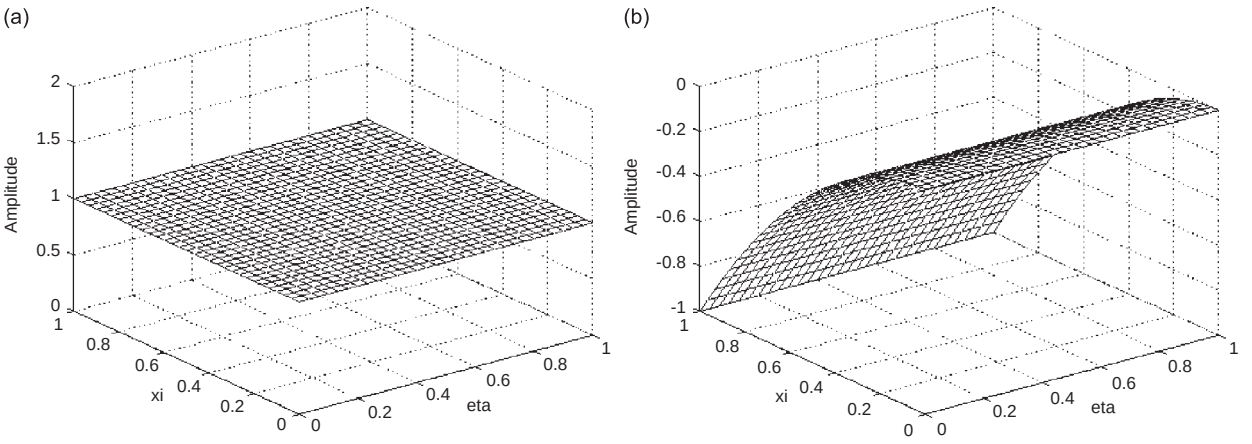

Fig. 13. Original load distributions: (a) for Case 5 and for the first frequency component in Case 6 and (b) for the second frequency component in Case 6.

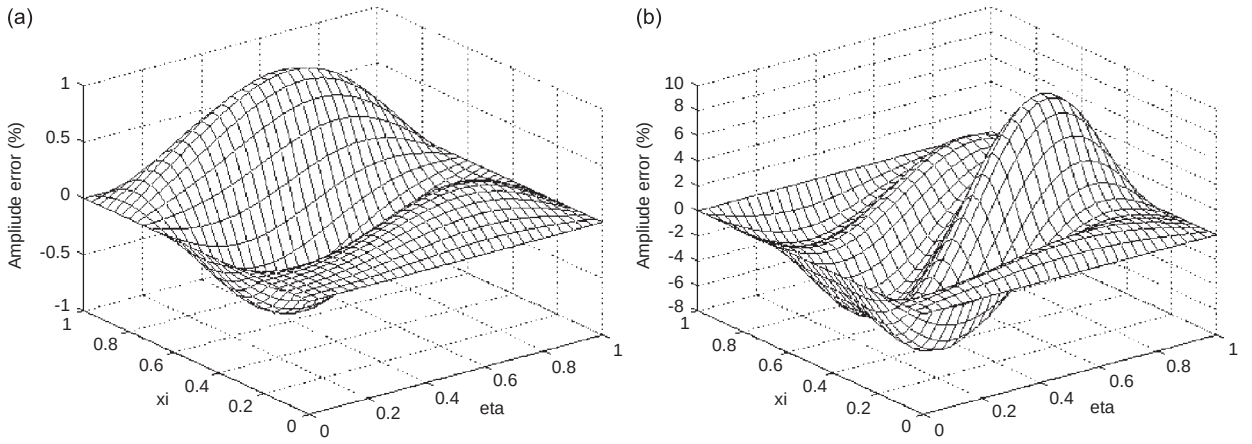

Fig. 14. Error distributions for Case 3: (a) for the first frequency component and (b) for the second frequency component.

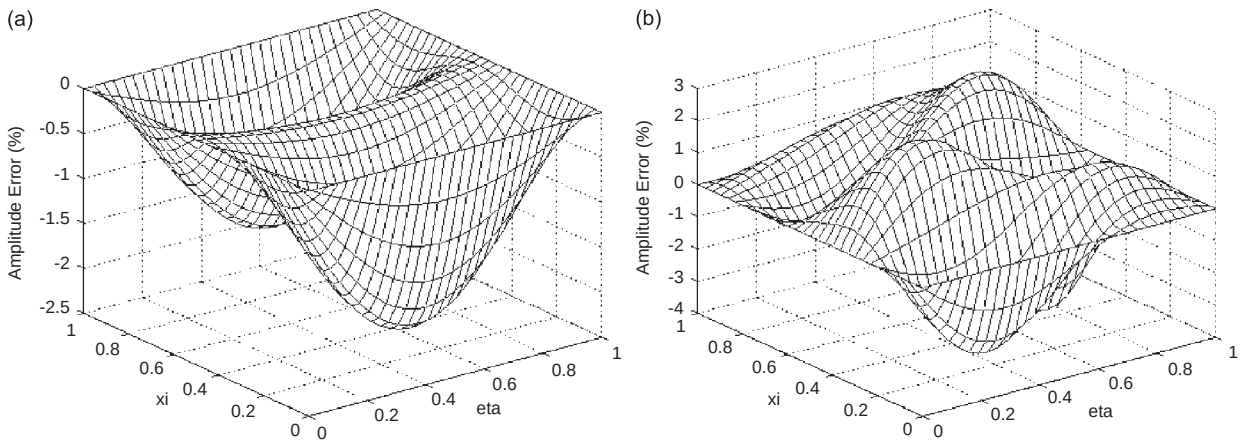

Fig. 15. Error distributions for Case 4: (a) for the first frequency component and (b) for the second frequency component.

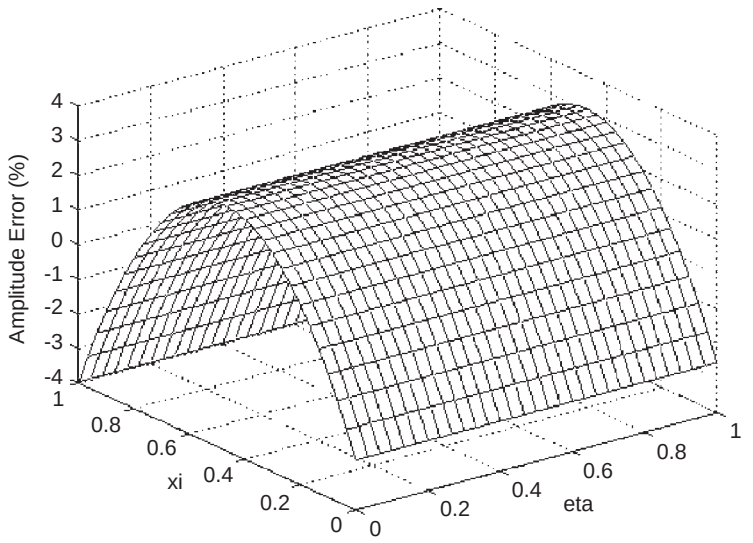

Fig. 16. Error distribution for Case 5.

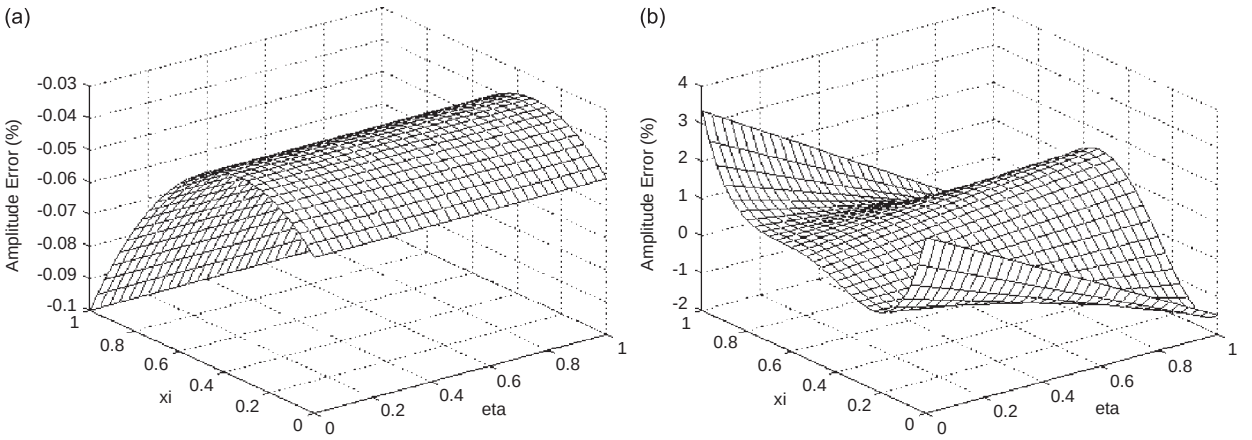

Fig. 17. Error distributions for Case 6: (a) for the first frequency component and (b) for the second frequency component.

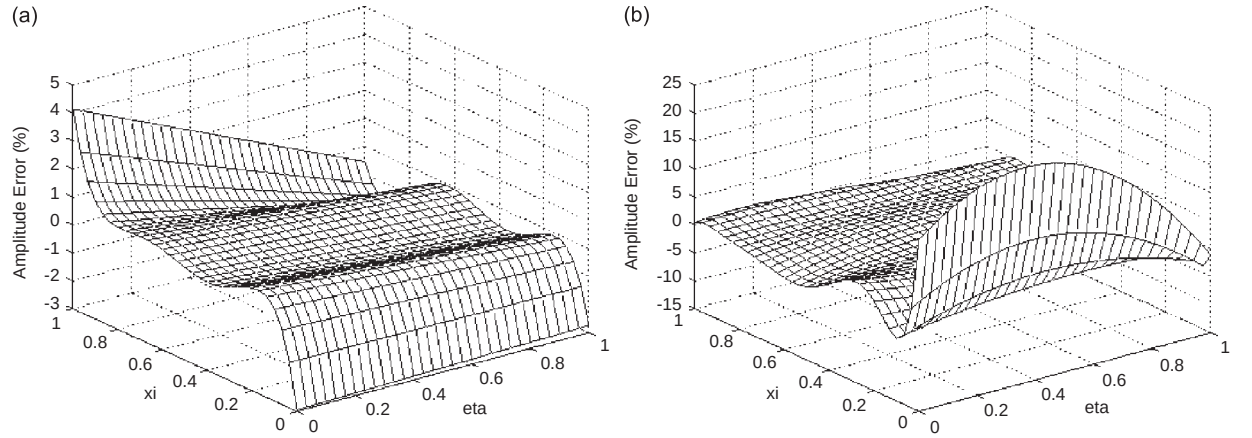

Fig. 18. Error distributions for Case 7: (a) for the first frequency component and (b) for the second frequency component.

Simulations in this subsection still display good accuracy even in complex situations provided that the noise levels are not too high.

5. Concluding remarks

In this study, the concept of scale factor and the method of mode selection are described with regard to a damped thin elastic plate, and the consequent reconstruction theory is proposed. To obtain the mode range for load reconstruction with anticipated error control, a criterion for the mode selection method is formulated.

Numerical simulations indicate that the load reconstruction has high accuracy even when the plate is under a complex distributed load. Simulation comparisons between the method of TSVD and the proposed method of mode selection demonstrate that the former is unstable probably due to its problem of selecting regularization parameter, while the latter is not only stable, but also robust. Moreover, the mode selection method can make a balance between the reconstruction range and error level.

The ongoing studies will focus on some open problems such as the improvement of the selection criterion and the relative high errors on boundaries.

References

[1] L.A. Lifschitz, C.E. D'Attellis, Input force reconstruction using wavelets with applications to a pulsed plasma thruster, *Mathematical and Computer Modelling* 41 (4–5) (2005) 361–369.

[2] J. Liu, C. Ma, I. Kung, D. Lin, Input force estimation of a cantilever plate by using a system identification technique, *Computer Methods in Applied Mechanics and Engineering* 190 (11–12) (2000) 1309–1322.

[3] M.T. Martin, J.F. Doyle, Impact force identification from wave propagation responses, *International Journal of Impact Engineering* 18 (1) (1996) 65–77.

[4] D.C. Kammer, Input force reconstruction using a time domain technique, AIAA-96-1201-CP.

[5] T.H.T. Chan, D.B. Ashebo, Theoretical study of moving force identification on continuous bridges, *Journal of Sound and Vibration* 295 (3–5) (2006) 870–883.

[6] S.S. Law, Y.L. Fang, Moving force identification: Optimal state estimation approach, *Journal of Sound and Vibration* 239 (2) (2001) 233–254.

[7] E.G. Yanyutin, A.V. Voropai, Identification of the impulsive load on an elastic rectangular plate, *International Applied Mechanics* 39 (10) (2003) 1199–1204.

[8] M. De Araújo, J. Antunes, P. Piteau, Remote identification of impact forces on loosely supported tubes—part 1: basic theory and experiments, *Journal of Sound and Vibration* 215 (5) (1998) 1015–1041.

[9] N.S. Vyas, A.L. Wicks, Reconstruction of turbine blade forces from response data, *Mechanism and Machine Theory* 36 (2) (2001) 177–188.

[10] M.C. Djamaa, N. Ouelaa, C. Pezerat, J.L. Guyader, Reconstruction of a distributed force applied on a thin cylindrical shell by an inverse method and spatial filtering, *Journal of Sound and Vibration* 301 (3–5) (2007) 560–575.

[11] Y. Liu, W.S. Shepard Jr., An improved method for the reconstruction of a distributed force acting on a vibrating structure, *Journal of Sound and Vibration* 291 (1–2) (2006) 369–387.

[12] N. Sehlstedt, A well-conditioned technique for solving the inverse problem of boundary traction estimation for a constrained vibrating structure, *Computational Mechanics* 30 (3) (2003) 247–258.

[13] C. Pezerat, J.L. Guyader, Force analysis technique: reconstruction of force distribution on plates, *Acta Acustica* 86 (2000) 322–332.

[14] S. Granger, L. Perotin, An inverse method for the identification of a distributed random excitation acting on a vibrating structure—part 1: theory, *Mechanical Systems and Signal Processing* 13 (1) (1999) 53–65.

[15] X.Q. Jiang, H.Y. Hu, Reconstruction of distributed dynamic loads on an Euler beam via mode-selection and consistent spatial expression, *Journal of Sound and Vibration* 316 (1–5) (2008) 122–136.

[16] H.G. Choi, A.N. Thite, D.J. Thompson, Comparison of methods for parameter selection in Tikhonov regularization with application to inverse force determination, *Journal of Sound and Vibration* 304 (2007) 894–917.

[17] H.G. Choi, A.N. Thite, D.J. Thompson, A threshold for the use of Tikhonov regularization in inverse force determination, *Applied Acoustics* 67 (7) (2006) 700–719.

[18] F.E. Gunawan, H. Homma, Y. Kanto, Two-step B-splines regularization method for solving an ill-posed problem of impact-force reconstruction, *Journal of Sound and Vibration* 297 (1–2) (2006) 200–214.

[19] J.W. Hilgers, B.S. Bertram, Comparing different types of approximators for choosing the parameters in the regularization of ill-posed problems, *Computers and Mathematics with Applications* 48 (2004) 1779–1790.

[20] D. Calvetti, S. Morigi, L. Reichel, F. Sgallari, Tikhonov regularization and the L-curve for large discrete ill-posed problems, *Journal of Computational and Applied Mathematics* 123 (2000) 423–446.

[21] S.H. Yoon, P.A. Nelson, Estimation of acoustic source strength by inverse methods—part II: experimental investigation of methods for choosing regularization parameters, *Journal of Sound and Vibration* 233 (4) (2000) 669–705.

[22] H. Lee, Y. Park, Error analysis of indirect force determination and a regularization method to reduce force determination error, *Mechanical Systems and Signal Processing* 9 (6) (1995) 615–633.

[23] K. Mosegaard, A. Tarantola, Monte Carlo sampling of solutions to inverse problems, *Journal of Geophysical Research* 100 (B7) (1995) 12431–12447.

[24] F. Kuhnet, *Pseudoinverse Matrizen und die Methode der Regularisierung*, Teubner-Texte zur Mathematik, Leipzig, 1976.

[25] T.Y. Xiao, S.G. Yu, Y.F. Wang, *Numerical Solution of Inverse Problems*, Science Press, Beijing, 2003 (in Chinese).

[26] J.G. Sun, *Matrix Perturbation Analysis*, Science Press, Beijing, 2001 (in Chinese).